ARMA 16-305

A Novel Mesh Generation Algorithm for Field-Level Coupled Flow and Geomechanics Simulations

Florez, Horacio A. and Ceberio, Martine
The University of Texas at El Paso, Department of Computer Science, Texas, USA

ABSTRACT: Generating a suitable hexahedral mesh for field-level coupled flow and geomechanics computation is still a challenging task. The lack of an analytical representation of the reservoir geometry makes generating a valid mesh for geomechanics a tedious and time-consuming endeavor. Indeed, usually the reservoir description comes as a static-model, i.e., corner-point geometry mesh, which is appropriate for flow simulations but not necessarily for mechanics. Having different meshes for flow and mechanics can alleviate this constraint but there is an intrinsic interpolation error in the procedure.

In order to minimize this error, we generate in the pay-zone region a mechanics mesh by smoothing the flow mesh. This procedure ensures that a valid mesh for finite element purposes is obtained and the projector, which maps pressures from the flow mesh into the generated reference mechanics mesh, is the identity matrix. This resulting pay-zone mesh is propagated into its surroundings by means of elliptical smoothing using linear elasticity. We also show that the same hexahedral mechanic pay-zone's mesh can be converted to a valid tetrahedral mesh by exploiting every hexahedron in a certain number of tetrahedrons. This latest procedure is attractive to bringing tetrahedral meshes into the picture, which allows treating constraints for the meshing process, i.e., faults and pitchouts, accordingly.

Finally, field-scale reservoir compaction and subsidence computations are carried out by using continuous Galerkin finite elements for mechanics, coupled with a slightly compressible single-phase flow simulator in order to demonstrate the applicability of the proposed algorithm.

1. BACKGROUND

Geomechanics at the reservoir level, i.e., reservoir compaction and subsidence, usually involves solving flow and mechanics by an iterative coupling technique [1-3]. This raises a question about what it is going to be a valid mesh for mechanics. At first glance, one may consider using the same mesh for flow and mechanics, at least in the so-called pay-zone. Meshing only in the pay-zone requires the in-situ stresses as Neumann boundary conditions, which is limited due to the uncertainties to measure them accurately in the field [4]. Another approach is to extend the reservoir mesh on its surroundings (i.e., non-pay-zone), which increases the computational cost by generating a large mesh for mechanics but it allows using simpler Dirichlet boundary conditions for displacements instead. This latter approach is more tractable in spite of its additional computational effort [1].

There exists a gap between static-model builders packages, such as Schlumberger's Petrel for instance, and mesh generators. Usually as a starting point, one may have a corner-point mesh for the pay-zone but neither geometrical nor analytical description of the reservoir itself [5]. This lack of representation makes generating a mesh in the non-pay-zone for mechanics a complicated and tedious task for most users. Another advantage of having such geometry is being able to generate a different mesh for mechanics even in the pay zone, which is quite attractive for several reasons such as having a coarser mesh for mechanics in the pay-zone or even non-matching meshes in the non-pay zone.

There have been significant efforts in recent years to generate hexahedral meshes and models suitable for coupled flow and mechanics simulations. Dean et al. [6] and Gai [7], for instance, embedded the flow mesh into a bigger conforming mechanics mesh and they set the porosity and permeabilities to zero outside the pay zone. Similarly, Schlumberger's Visage/Virage geomechanics solution also follows an approach based on embedding [5]. They manage to extend the reservoir mesh towards the surroundings by claiming that the pay zone mesh is exactly honored. For general reservoir meshes with faults and pitchouts, that claim cannot be made because some hexahedral elements degenerate (due to pitchouts, for instance), and faults must be smoothed out to avoid dealing with contact problems on those discontinuous surfaces. Angus et al. [8] followed a similar approach pointing out that the resulting mechanics mesh must be watertight, meaning that there must be no gaps in the mesh, and each node must be connected to neighboring nodes properly. For them, faults and other subsurface discontinuities pose a major challenge, and thus they must be properly handled when exported from the geological model. On the other hand, Lie et al. [9] recognized the necessity of employing unstructured meshes when dealing with complex geological features and also to overcome limitations in the numerical schemes such as K-orthogonal grids. Mustapha [10] developed a mesh generation tool aimed to tackle complex fractured geological media by using triangular/tetrahedral grids. Also, Juntunen and Wheeler [11] employed modern mesh generation techniques to improve the quality of the resulting mesh while reducing the number of elements and capture the geometry accurately by using orthogonally optimized hexahedral meshes. These approaches based on unstructured and more general hexahedral meshes suggest different meshes for flow and mechanics in the pay zone.

The remainder of the paper is organized as follows. Section 2 presents the mathematical model and the governing partial differential equations. Section 3 focuses on the mesh generation process based on the elasticity operator. Section 4 discusses how to attract the mesh towards given features by using a pressure-drop as driving force. In Section 5, we present concrete numerical examples of mesh generation and coupled flow, and geomechanics simulations are conducted to demonstrate the applicability of the methodology proposed in this paper. Finally, Sections 6 and 7 state concluding remarks and future work respectively.

2. MATHEMATICAL MODEL

This section discusses the governing equations for linear homogeneous isotropic poroelasticity and their finite element formulation. We omit details for the sake of brevity, a more detailed treatment can be found [4]. We consider a bounded domain $\Omega \subset \Re^{2,3}$ and its boundary $\Gamma = \partial\Omega$. Let ξ_h be a non-degenerate, quasi-uniform conforming partition of Ω composed of quadrilaterals or hexahedrons. For the elasticity part, we start from the equilibrium equation for a quasi-steady process:

$$-\nabla \cdot \underline{\underline{\sigma}} = \underline{0} \text{ in } \Omega \; ; \; \Gamma = \Gamma_D^u \cup \Gamma_N^u \; ; \qquad (1)$$
$$\underline{\boldsymbol{u}} = \underline{0} \text{ on } \Gamma_D^u \; ; \; \underline{\boldsymbol{t}} = \underline{\underline{\sigma}} \cdot \underline{\hat{n}}, \text{ on } \Gamma_N^u \; ,$$

where $\underline{\underline{\sigma}}$ is the stress tensor, $\underline{\hat{\boldsymbol{n}}}$ is the outer normal unitary vector. The boundary conditions for mechanics can be assumed to be of Dirichlet type on Γ_D^u, and Neumann type on $\Gamma_N^{\boldsymbol{u}}$, where the external tractions are prescribed. Hooke's law and Biot's poroelastic theory define $\underline{\underline{\sigma}}$ by [4]:

$$\underline{\underline{\sigma}} = \underline{\underline{C}} : \underline{\underline{\varepsilon}} - \alpha\left(p - p^0\right)\underline{\underline{\delta}} \; ; \; \underline{\underline{C}} = \lambda \underline{\underline{\delta}} \otimes \underline{\underline{\delta}} + 2\mu \underline{\underline{\Pi}} \; . \qquad (2)$$

Where $\underline{\underline{\boldsymbol{C}}}$ is the elastic moduli of isotropic elasticity, $\underline{\underline{\delta}}$ is the Kronecker delta, and λ, μ are the Lamé constants, and $\underline{\underline{\Pi}}$ is the fourth-order identity tensor. The strain tensor $\underline{\underline{\varepsilon}}$ is defined by:

$$\underline{\underline{\varepsilon}} = \nabla^s \underline{\boldsymbol{u}} = \frac{1}{2}\left[\nabla \underline{\boldsymbol{u}} + \left(\nabla \underline{\boldsymbol{u}}\right)^T\right] . \qquad (3)$$

The Lamé constants can be expressed regarding familiar quantities such as Young's Modulus, E, and Poisson ratio, ν [4]:

$$\mu = G = \frac{E}{2\left(1+\nu\right)} \; ; \; \lambda = \frac{E\nu}{\left(1+\nu\right)\left(1-2\nu\right)} \qquad (4)$$

where $\boldsymbol{G}$ is the Shear Modulus [4].

For the flow part, we are interested in the steady-state continuity equation [4], this is:

$$\nabla \cdot \left(-\frac{1}{\mu}\underline{\underline{\boldsymbol{K}}} \cdot \nabla p\right) = 0 \; , \qquad (5)$$

where $\underline{\underline{\boldsymbol{K}}}$ is the absolute permeability tensor, μ is the dynamic viscosity, and $\boldsymbol{p}$ is the fluid. The typical boundary conditions for pressure involve Neumann or no-flow namely:

$$\nabla p \cdot \underline{\hat{n}} = 0 \; .$$

We derive weak forms for Eq. (1) and (2) by multiplying by a test function, $v \in H_0^1\left(\Omega\right)$, and integrating over the domain and applying the Gauss divergence theorem. We omit details here for the sake of brevity; a more detailed treatment can be found in [1-4]. This leads to our finite element model for steady state linear isotropic poroelasticity:

$$\begin{bmatrix} \underline{\underline{K}} & -\underline{\underline{Q}} \\ 0 & \underline{\underline{H}} \end{bmatrix} \begin{Bmatrix} \underline{\boldsymbol{u}} \\ \underline{\boldsymbol{p}} \end{Bmatrix} = \begin{Bmatrix} \underline{\boldsymbol{f}_u} \\ \underline{\boldsymbol{f}_p} \end{Bmatrix} , \qquad (6)$$

where the matrices are given by:

$$\underline{\underline{K}} = \int_{\Omega} \underline{\underline{B}}^T \underline{\underline{C}}\ \underline{\underline{B}} dx\ ;\ \underline{\underline{Q}} = \int_{\Omega} \underline{\underline{B}}^T \alpha \boldsymbol{m}\ \underline{\Pi} dx\ ;\ \boldsymbol{m} = (1,1,0)^T\ ;$$

$$\underline{\boldsymbol{f}_p} = \int_{\partial\Omega_N^p} \left(\frac{1}{\mu} \underline{\underline{\boldsymbol{K}}} \nabla p \cdot \boldsymbol{n} \right) \cdot \underline{\psi}_p\ ds\ ;\ \underline{\boldsymbol{f}_u} = \int_{\partial\Omega_N^u} \boldsymbol{t} \cdot \underline{\underline{\Psi}}^T\ ds\ ;$$

$$\underline{\underline{H}} = \int_{\Omega} \frac{1}{\mu} \underline{\underline{\boldsymbol{K}}} \nabla \underline{\Pi} \cdot (\nabla \underline{\Pi})^T dx\ . \tag{7}$$

where $\underline{\Pi}$ and $\underline{\underline{\Psi}}$ are matrices of shape functions [12,4]. The system (6) can be decoupled in different ways [3]. The loose coupling approach consists of taking the pressures $\underline{p}$, to solve for displacements $\underline{\boldsymbol{u}}$:

$$\underline{\underline{K}} \cdot \underline{\boldsymbol{u}} = f_u + \underline{\underline{Q}} \cdot \underline{p}\ . \tag{8}$$

3. MESH GENERATION BY ELASTICITY

Our extensive experience with coupled flow and geomechanics simulations told us a long time ago that the elasticity differential operator (1) can generate smooth meshes similarly to the elliptic methods based on nonlinear PDEs [13]. The radical difference lies in the fact that the operator (1) is still linear for linear isotropic elasticity, which reduces the computational cost of generating a curvilinear system of coordinates, i.e., mesh generation, to solving a linear system of equations.

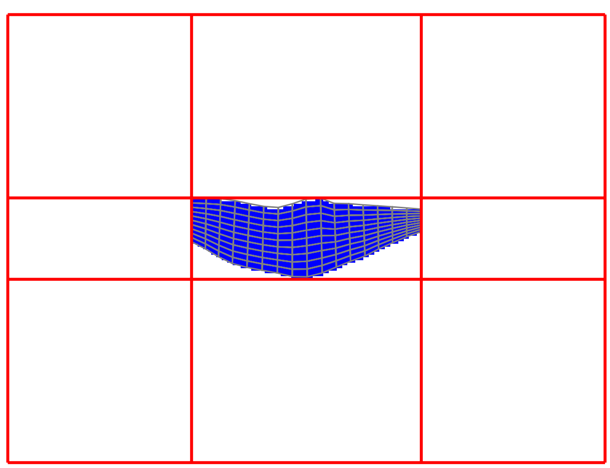

Fig. 1. The smoothed pay zone mesh and the skeleton polygon are depicted.

We propose an algorithm that relies on our previous works on ARMA paper 13-476 [14] and its polished journal version [15]. We refer the reader to those papers for a full explanation of the present algorithm's foundations. We assume as inputs a smoothed pay zone mesh and reconstruction's skeleton polygon. Figure 1 shows both inputs in the computational space where the skeleton polygon is aligned with the coordinates axis. We derive a smoothed pay zone mesh by smoothing the inputted corner-point geometry mesh, and then attracting the capture polygon towards the reservoir as described in [15].

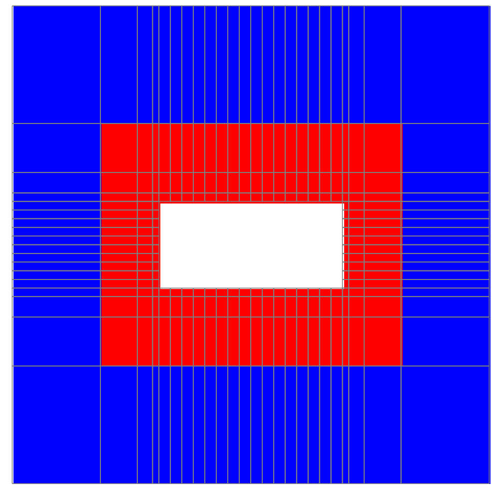

Fig. 2. It shows the reference mesh and difference regions for having different properties. There is a hole in the center.

We now want to solve the problem (1) on the normalized reference mesh shown in Figure 2, which has a hole in the center. The reference mesh in Figure 2 was generated by bilinear interpolation from the skeleton reference points. The mesh size is *Nx* = 16, *Ny* = 10, on the sideburdens we have *Ns* = 4 (sideburden direction), where *Nx, Ny* and *Ns* are the numbers of elements in their respective directions. We tackle here a coarse mesh for simplicity so that the figures do not get saturated. However, the present algorithm is not limiting in that regard. We also generated a coarser version of the sample reservoir in Figure 1 (see Section 5 for details); we assume that this is our reference pay zone mesh. We employed blending function described in [15] to attract the mesh towards the hole. We enforce far field boundary conditions in the domain's outer faces, i.e., displacements in the perpendicular direction are set to zero, while in the hole, the displacements are prescribed to be the difference between the reference's mesh points and their counterpart in the target pay zone mesh. This latest condition guarantees that the generated mesh exactly honors the pay zone mesh. Since the system (1) is coupled, this will also move the interior points of the domain that are not constrained.

Figure 3 shows results for the following mechanical properties; $E_{red} = 0.5$, $E_{blue} = 0.001$, $\nu = 0.3$, where we assume consistent pressure and length units, for instance, MPa and meters. We observe that the generated mesh is pulled towards the pay zone as expected. The magnitude of the movement is a function of the contrast of Young modulus between the red and blue regions in Figure 2. We then generate the final mesh by merging the mesh in Figure 3 with the source pay zone mesh. We will further study the influence of the mechanical properties in the shape of the resulting mesh in a forthcoming journal paper.

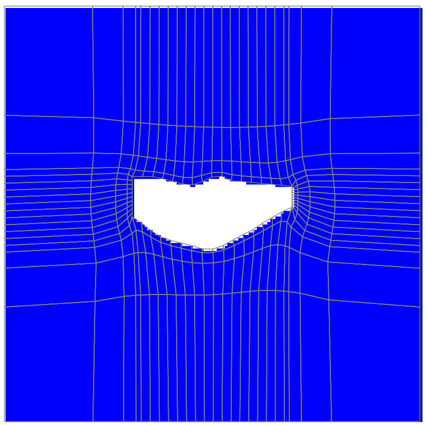

Fig. 3. The figure shows the solution to the problem (1) subject to Dirichlet boundary conditions in the hole.

4. MESH ATTRACTION BY PRESSURE

We noticed that pressure-drop loading in (1) could also play the role of attracting the mesh towards given features. To demonstrate that, we solve (5) on the mesh in Figure 2, subject to no-flow boundary conditions at the outer edges while in the hole, the pressure is assumed to be minus one. We utilize the following permeabilities in md,

$$K_x^{red} = K_y^{red} = 0.01,\ K_x^{blue} = K_y^{blue} = 0.0001 .$$

Figure 4 presents the solution flow field.

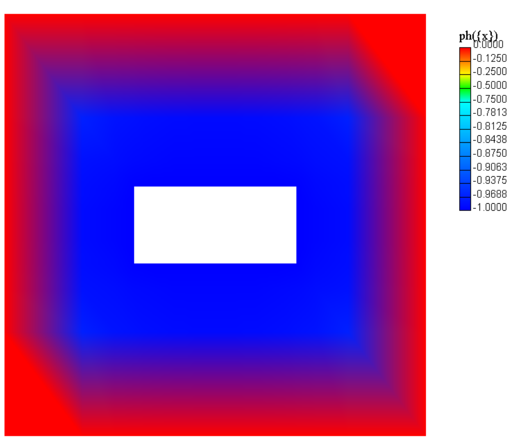

Fig. 4. This pressure profile resolves problem (5) subject to given boundary conditions.

We now solve (1) in loose coupling fashion (8), while using the above pressure field as the driving force. Far field boundary conditions were assumed in the outer edges while the hole is considered to be traction free. Figure 5 depicts the solution displacement field, i.e., the generated mesh.

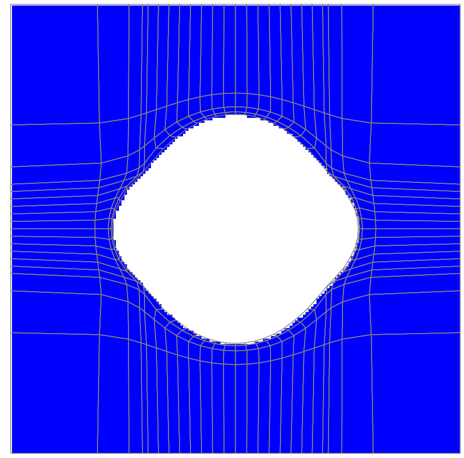

Fig. 5. Taking a pressure field in Figure 4, as the driving force, generated this mesh.

5. NUMERICAL EXAMPLES

This reconstruction algorithm was implemented in the object-oriented program “Adhora - LogProc v1.0” which is a parallel C++ OpenGL application. We present three examples in this section; the first one reconstructs a given reservoir dataset, by running the two-dimensional version of the proposed algorithm and then it performs a coupled flow and mechanics simulation to demonstrate the usability of the generated mesh. The second example extends the treatment to a three-dimensional problem and also conducts a finite element simulation. The third example discusses how to bring unstructured tetrahedral meshes into the picture.

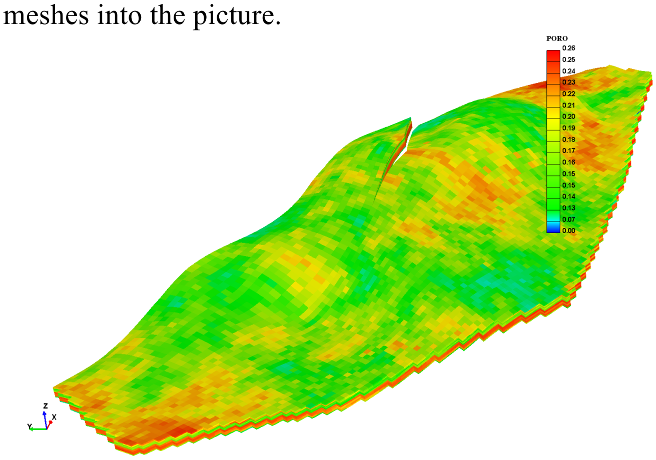

Fig. 6. Brugge Field geometry, showing the porosity field, is depicted (The plot is exaggerated seven times in the vertical direction).

A well-known open-to-the-public reservoir dataset is reconstructed to show that the present algorithm can deal with problems of practical interest. The input dataset corresponds to the Brugge Field, which is synthetic oil field dataset that was constructed to propose a benchmark case for closed-loop reservoir management [16]. This latter model is the basis for a series of realizations to be used in reservoir simulations. The Brugge source model, shown in Figure 6, consists of 60048 hexahedral elements corresponding to a mesh of size Nx = 139, Ny = 48, Nz = 9. A tensor product capture-polygon 34 × 12 was used to represent the reservoir's topology.

All FEM computations were carried out by using the geomechanics simulator so-called "IPFA" that stands for Integrated Parallel Finite Element Analysis program, which is a parallel C++ application being developed the leading author. IPFA's main characteristics can be found in these references [4,17-20]. All examples included here were run on a MacBook Pro laptop equipped with an Intel(R) Core(TM) i7-2720QM CPU @ 2.20GHz and 8 GB of RAM.

5.1. Example 1: Reservoir Cross-Section mesh and Coupled Flow and Mechanics Simulation.

We employ extrapolation lengths of 0.8 · L on the side-burdens, where L is the reservoir length, to obtain the skeleton shown in Figure 1. We populate the smoothed pay zone mesh with porosity and permeability data that comes from the SPE 10 Comparative Solution Project, this for the sake of simplicity. The boundary conditions for mechanics are depicted in Figure 7 while no-flow on all reservoir faces are assumed for the pressure equation.

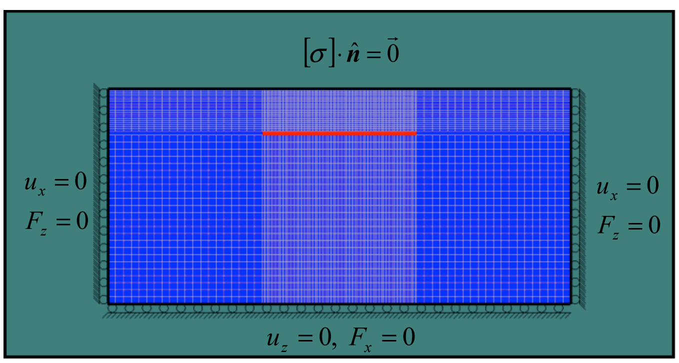

Fig. 7: The boundary conditions for the mechanics problem in the *x-z* plane are depicted (the pay zone is highlighted in red color).

The initial pressure is assumed constant equals to 10000 Psi while the pressure in the producer wells is assumed at 9000 Psi, which corresponds to a depletion scenario. The BC for mechanics are the typical ones for these problems: traction free on the top surface, no horizontal displacement on the side planes and no vertical displacement on the bottom surface and the initial displacement field is assumed to be zero. We considered linear isotropic elasticity with mechanical properties for both the reservoir and its surroundings given by E = 30 ksi and ν = 0.3. The fluid viscosity is 0.1325 cp, and its Biot Modulus is 357142.85 Psi^{-1}. No gravity loading was considered for both flow and mechanics.

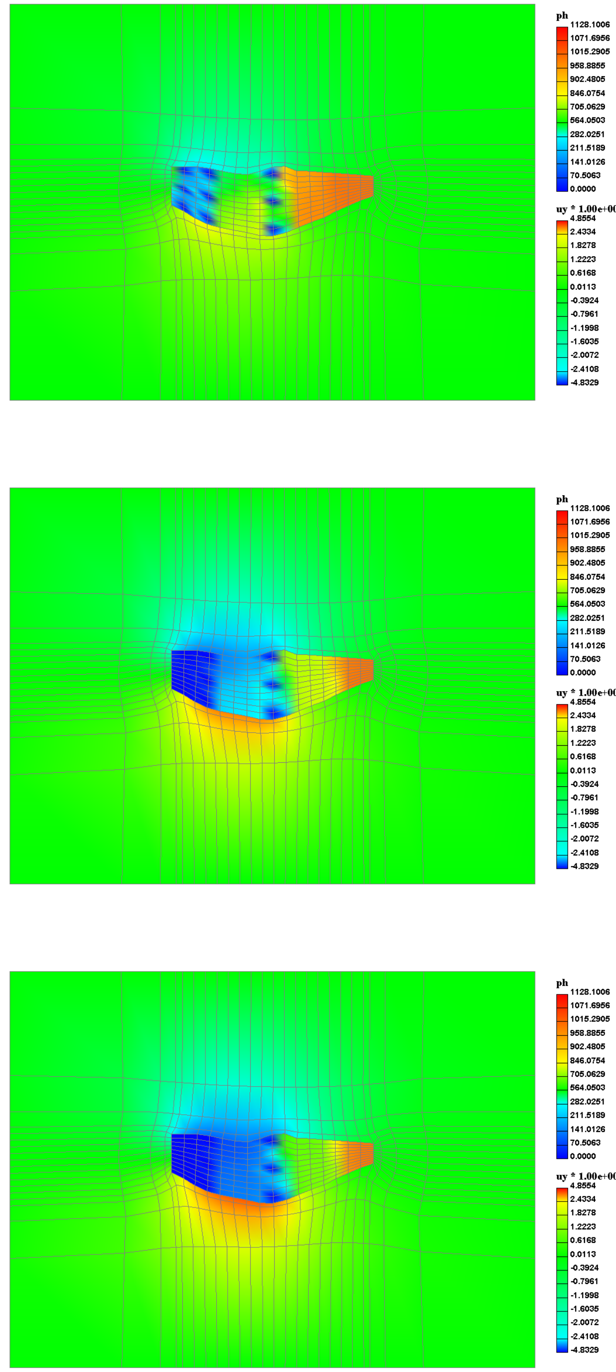

Fig. 8. This shows pressure and vertical displacement u_y, field snapshots after 10, 30 and 40 years of evolution simultaneously, from top-to-bottom. Only the pressure variation above 9000 Psi is shown.

Figure 8 presents the results for a plane-strain coupled flow and geomechanics simulation with the generated mesh that also included the pressure-drop attraction effect. We clearly observe the classical pattern of deformation outside the pay zone, with a build up on the bottom and a compaction dome on the top. The reservoir's depletion induces these deformations. These results demonstrate the applicability of the generated two-dimensional mesh.

5.2. *Example 2: 3-D Reconstruction and Coupled Flow and Mechanics Simulation.*

We now extend the previous example to three-dimensions. Also, we consider the extrapolation lengths of $15 \cdot H$ on the over- and under-burden respectively, where H is the reservoir thickness, to compute the skeleton polygon. The additional mesh sizes are $Nz = 4$, $Nu = 5$, $No = 3$, where "u" and "o" stand for under- and over-burden respectively. Figure 9 depicts the reference geomechanics mesh that will be deformed to honor the pay zone constraint. In this case, we do not have a hole in the middle, for simplicity, all points lying in that interior patch would be moved by imposing Dirichlet boundary conditions, so that inner mesh matches exactly the smoothed pay zone mesh.

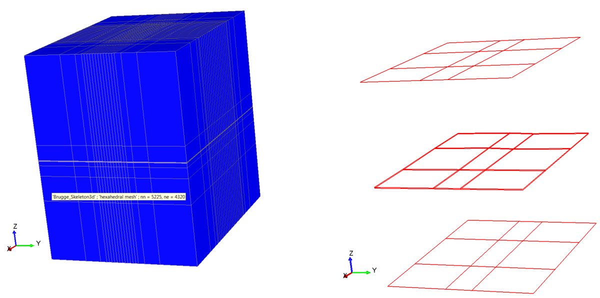

Fig. 9. It shows reference 3-D mesh (right) and its skeleton (left), where we employed blending to attract it towards the pay zone.

It is also possible to impose the 2-D mesh as a pillar for a two and a half 3-D mesh; we rather want to proceed to the full 3-D problem. This latest approach may be cumbersome if the final mechanics mesh needs to be imported into software that relies on the pillar approach. Notice that this mesh is general hexahedral and thus, it can violate the pillar hypothesis.

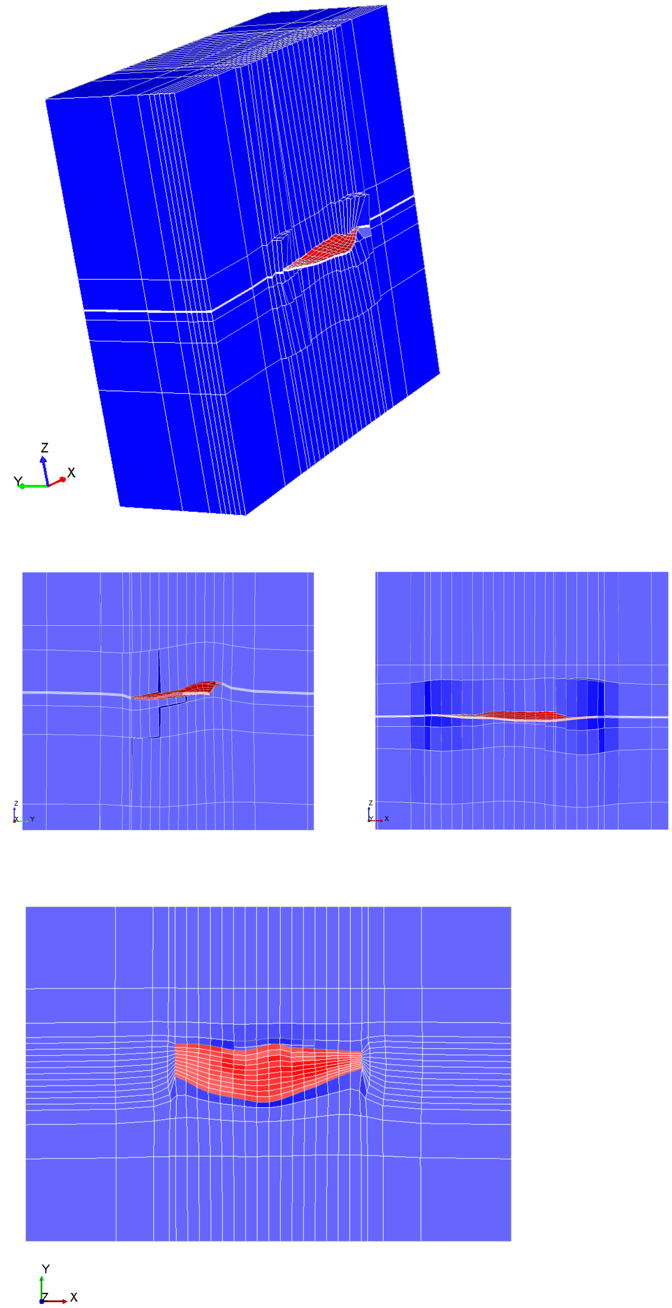

Fig. 10. The figure shows the solution to the 3-D problem (1) subject to the pay zone mesh constraint, which is highlighted in red.

Figure 10 shows the resulting mesh. We have a cut-away view of the half mesh in the top, and cross-sections in *z*-, *y*- and *x*-planes respectively in the bottom. The mesh from a top view looks alike with its 2-D counterpart. However, we notice deformation in the other planes; the elements tend to curve and incline as well. This general hexahedral mesh would be challenging to fit into the pillar approach, i.e. two and half approach.

We now conduct a similarly coupled flow and geomechanics simulation such as the one performed in the previous section. We populate the model in the same fashion, and we apply the same boundary and initial conditions. We consider the same homogeneous mechanical properties.

Figure 11 shows pressure snapshots after 40 years of evolution. These correspond to increasing times from top-to-bottom. The reservoir slowly depletes which causes the pressure to drop as shown. Figure 11 also depicts the vertical displacement u_z, which reproduces a similar compaction area (blue area) propagating from the reservoir to the surface. That compaction dome grows as the pressure drops. There is also a build-up in the bottom face of the reservoir. This behavior corresponds the classical deformation in a reservoir being subjected to compression due to the pressure drop, which shows that the generated mesh is a valid mesh for finite element purposes.

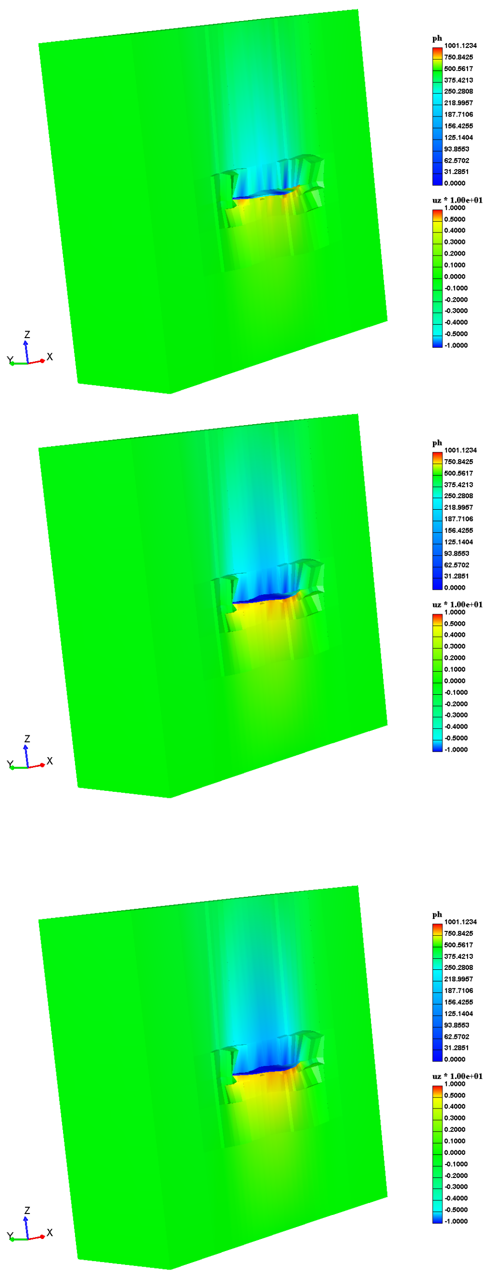

Fig. 11. This figure shows pressure and vertical displacement u_z, field snapshots after 10, 30 and 40 years of evolution, from top-to-bottom. Only the pressure variation above 9000 Psi is shown. The plot is exaggerated three times in the vertical direction.

5.3. *Example 3: Considering Unstructured Meshes.*

We now want to bring tetrahedral meshes into the picture. One challenge that immediately emerges is the aspect ratio of the reservoir. i.e. thickness to length ratio that makes generating a tetrahedral mesh in the pay zone cumbersome. Another constraint to consider is preserving the source hexahedral mesh so pressures can be mapped in a straightforward manner from the pay zone into the resulting mechanics mesh. For these reasons, we exploit every hexahedron in the pay zone into eight tetrahedrons as shown in Figure 12.

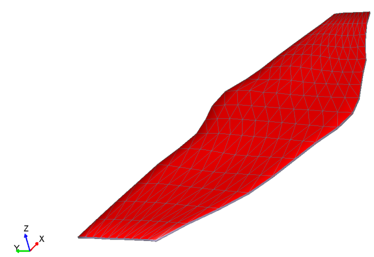

Fig. 12. This figure shows R-trians in the pay zone surface mesh.

We then generate a triangular surface mesh in the outer box represented by the reconstruction skeleton. We then generate a tetrahedral mesh where the pay zone is considered to be a hole; this renders the final tetrahedral mesh that is depicted in Figure 13. This simple procedure opens new avenues for bringing unstructured meshes in the coupled flow and geomechanics field level simulations. Faults and another feature can be properly considered within this framework. We will further elaborate on this topic in a separate upcoming paper.

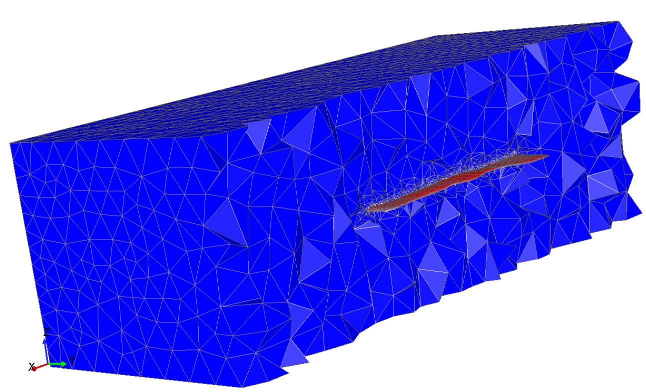

Fig. 13. This figure depicts the final tetrahedral mesh.

6. CONCLUSIONS

A new algorithm able to reconstruct a given oil reservoir geometry has been developed and applied to a real dataset:

1. Graphical examples were presented to demonstrate the concepts used in this research.
2. We provide new perspectives on the approximation of realistic reservoir geometries and mesh generation in the context of coupled flow and geomechanics.
3. The finite element computations demonstrated that this reconstruction procedure is quite useful to deal with realistic reservoir compaction and subsidence simulations.

7. FUTURE WORK

We have some pending tasks in the queue already to keep on going with this research such as:

1. Finalizing the algorithm's implementation in "LogProc" by providing a proper graphical user interface and options for end users. Performing further testing with other open-to-the-public datasets that are already available.
2. Developing a version that can generate non-matching meshes, i.e., coarser aerial meshes in the over- and under-burden would be helpful to reduce the computational cost. These subdomains can be glued together by using the Mortar-FEM method. This is the ultimate goal. The idea is to get rid of tensor product meshes to have different meshes on different domains, such as the reservoir and its surroundings.

REFERENCES

1. Florez H.A., M.F. Wheeler, A. Rodriguez, and J.E.P. Monteagudo. 2011. Domain Decomposition Methods Applied to Coupled Flow-Geomechanics Reservoir Simulation. In *Proceedings of the SPE Reservoir Simulation Symposium*. Paper 141596. The Woodlands.
2. Florez H.A., Wheeler M.F. and Rodriguez A. 2013. Domain Decomposition Methods in Geomechanics. In *SPE Reservoir Simulation Symposium*. Paper 163674. The Woodlands.
3. Kim J., H.A. Tchelepi, and R. Juanes. 2009. Stability, Accuracy and Efficiency of Sequential Methods for Coupled Flow and Geomechanics. In *Proceedings of the SPE Reservoir Simulation Symposium*. Paper 119084. The Woodlands.
4. Florez H.A. 2012. *Domain Decomposition Methods for Geomechanics*. Ph.D. Dissertation: The University of Texas-Austin.
5. Schlumberger. 2007. ECLIPSE File Formats 2007.1 Reference Manual. Copyright 1991-2007 Schlumberger.
6. Dean R., Gai, X., Stone, C., Minkoff, S. 2003. A comparison of techniques for coupling porous flow and geomechanics. No. 79709 in SPE Reservoir Simulation Symposium. SPE, Houston.
7. Gai, X. 2004. A coupled geomechanics and reservoir flow model on parallel computers. Ph.D. thesis, The University of Texas at Austin.
8. Angus, D., Verdon, J., Fisher1, Q., Kendall, J., Segura, J., Kristiansen, T., Crook, A., and J. Yu, S.S., Dutko, M. 2011. Integrated fluid-flow, geomechanics and seismic modeling for reservoir characterisation. Focus Article coordinated by Kurt Wickel, pp. 27–35. UK.
9. Lie, K., Krogstad, S., Ligaarden, I.S., Natvig, J.R., Nilsen, H.M., Skaflestad, B. 2012. Open-source Matlab implementation of consistent discretizations on complex grids. Computational Geosciences 16, 297–322.
10. Mustapha, H. 2011. G23fm: a tool for meshing complex geo- logical media. Computational Geosciences 15, 385–397.
11. Juntunen, M., Wheeler, M.F. 2013. Two-phase flow in complicated geometries. Computational Geosciences 17, 239– 247.
12. Becker E.B., G.F. Carey, and J.T. Oden. 1981. *Finite Elements: An Introduction*. Volume I of The Texas Finite Element Series. New Jersey: Prentice-Hall Inc., Englewood Cliffs.
13. Thompson, J.F., B.K. Soni, and N.P. Weatherill. 1999. *Handbook of Grid Generation*. Boca Raton: CRC Pres.
14. Florez H.A., J. Florez and R. Manzanilla, 2013, "Oil Reservoir's Geometry Reconstruction and Mesh Generation by Using NURBS Surfaces", ARMA 13-476, 47th US Rock Mechanics / Geomechanics Symposium held in San Francisco, CA.
15. Florez H.A., R. Manzanilla, J. Florez, and M.F. Wheeler, 2014, "Spline-based reservoir's geometry reconstruction and mesh generation for coupled flow and mechanics simulation", Computational Geosciences, DOI 10.1007/s10596-014-9438-7, SSN 1420-0597, Springer International Publishing, pp. 1-19.
16. Geel K. 2009. Description of the Brugge field and property realizations. Bruges, Belgium: TNO.
17. Florez H.A. 2013. A mortar method based on NURBS for curved 3-D interfaces. In *47th US Rock Mechanics/Geomechanics Symposium*. Paper 475. San Francisco.
18. Florez H.A., M.F. Wheeler, and A. Rodriguez. 2012. A mortar method based on NURBS for curved interfaces.

In *46th US Rock Mechanics/Geomechanics Symposium*. Paper 313. Chicago.

19. Florez H.A., M.F. Wheeler, and A. Rodriguez. 2012. A mortar method based on NURBS for curved 3-D interfaces. In *Proceedings of the 13th European Conference on the Mathematics of Oil Recovery (ECMOR XIII)*. France.

20. Florez H.A., 2013, "A mortar method based on NURBS for curved 3-D interfaces", ARMA 13-475, 47th US Rock Mechanics / Geomechanics Symposium held in San Francisco, CA.